Supplementary Information (SI) for ChemComm.
This journal is © The Royal Society of Chemistry 2026

Interchromophoric Excitonic Coupling Controls Phosphorescence in Thermomorphs of Carbazole Dimer

Jibin Sivanarayanan[a], Abhijith Muralidharan[a], Amalnadh T[a]. and Mahesh Hariharan[a]*

[a] School of Chemistry, Indian Institute of Science Education and Research Thiruvananthapuram (IISER TVM), Maruthamala P. O., Vithura, Thiruvananthapuram-695551, Kerala, India.

*E-mail: mahesh@iisertvm.ac.in

Supporting Information (SI)

Table of Contents

Section 1: Materials and Methods

All chemicals were procured from commercial suppliers and utilised as received without further purification. All reactions were carried out in oven-dried glassware prior to use. Solvents were dried and distilled by standard laboratory purification techniques. TLC analyses were performed on recoated aluminium plates of silica gel 60 F254 plates (0.25 mm, Merck), and developed TLC plates were visualised under short- and long-wavelength UV lamps. Column chromatography was performed using silica gel 200-400 mesh, employing a solvent polarity corresponding to the TLC mobility of the substance of interest. Yields are reported for substances that are chromatographically and spectroscopically homogeneous. Melting points were determined using a capillary melting point apparatus. ^{1}H and ^{13}C NMR spectra were recorded on a 500 MHz Bruker Advance DPX spectrometer, with tetramethylsilane (TMS) as the internal standard. Mass spectra were obtained using a Bruker UltrafleXtreme MALDI-TOF/TOF with Matrix Assisted Laser Desorption/Ionisation (MALDI). Photophysical measurements of the derivatives were performed in a 10 mm path-length cuvette. Absorption and emission spectra were recorded on Shimadzu UV-3600 UV-VIS-NIR and Horiba Jobin Yvon Fluorolog spectrometers, respectively. Fourier transform infrared spectroscopy (FTIR) measurements were recorded on a Shimadzu IR Prestige-21 FTIR spectrometer as KBr pellets.

1.1 Computational Analysis

All the calculations were carried out in Gaussian 16.[1] Ground-state geometry optimisation in vacuum was performed at CAM-B3LYP-D3/def2-SVP level of theory. Vertical excitation energies and oscillator strengths were calculated employing time-dependent DFT (TD-DFT) at the CAM-B3LYP-D3/def2-SVP level of theory. To compute long-range Coulombic coupling, an electronic energy transfer (EET) module in Gaussian 16 was utilised. Electron and hole transfer coupling values were calculated by employing the CATNIP Tool version 1.9.9. Both Multiwfn and CATNIP use post-processed Gaussian 16 output files for the respective analyses. To compute long-range Coulombic coupling, an electronic energy transfer (EET) module in Gaussian 16 was utilised.

1.2 Potential Energy Surface

The PES scan was carried out by incrementally varying the dihedral angle while keeping the remaining atomic coordinates fixed, and the corresponding energies were calculated for each geometry. This analysis provides a direct picture of how torsional rotation influences molecular potential energy, enabling the identification of energetically preferred conformations and regions associated with higher rotational barriers. The scan, therefore, offers qualitative insight into the conformational energy landscape of the molecule.[2]

1.3 X-ray Crystallography

High-quality crystals with appropriate dimensions were selected for the X-ray diffraction experiments.

The crystallographic data collected are presented in Tables S1& S2 of the Supporting Information. A single crystal was mounted using oil (Infineum V8512) on a glass fiber. All measurements were made using a CCD area detector with graphite-monochromated Mo Kα radiation. The data were collected with the Bruker APEXII detector and processed with APEX2 from Bruker. The structure was solved by the direct method and expanded using the Fourier technique. The non-hydrogen atoms were refined anisotropically. Hydrogen atoms were included in idealised positions but not refined. Their positions were constrained relative to their parent atom using the appropriate HFIX command in SHELX-97.1.1.[3] All programs used during the crystal structure analysis are incorporated in the WINGX software.[4] The full validation of CIF and structure factor was performed using the checkCIF utility. The 3D structure was carried out using Mercury 3.10.1.4.[5]

Arithmetic & simple metrics

V(298 K) = 1437 Å³ → V(77 K) = 1387 Å³):

- Absolute change ΔV = 1437 − 1387 = 50 Å³.
- Fractional change = 50 / 1437 = 0.0348 = 3.48% volume decrease.
- Temperature change ΔT = 77 − 298 = −221 K.

Volumetric thermal expansion coefficient (approximate, using average V):

$$\beta \approx \frac{\Delta V}{\bar{V}\,\Delta T} = \frac{-50}{1437 \times (-221)} \approx 1.60 \times 10^{-4}\ K^{-1}.$$

Convert to an effective linear thermal expansion (≈ β/3):

$$\alpha_{linear} \approx \frac{\beta}{3} \approx 5.3 \times 10^{-5}\ K^{-1}.$$

These numbers are well within typical ranges for organic molecular crystals (linear α often ~10^{-5}–10^{-4} K^{-1}). So a ~3.5% volume contraction on cooling from 298→77 K is thermally plausible.

1.4 SAPT(0)

SAPT(0) analysis was employed to determine the non-covalent interaction energies of dimer molecules. The SAPT module of the psi4 code was employed, with a 6-31G(d,p) basis set.[6] SAPT(0) calculations provide the contributing components of interaction energy. The results from the SAPT(0) analysis are a second-order perturbation expansion, consisting of first-order electrostatic and exchange energy terms and second-order dispersion, induction, and their exchange counterparts as perturbation terms.

$$E_{int}^{SAPT(0)} = E_{elec}^{(1)} + E_{ex}^{(1)} + E_{ind}^{(2)} + E_{ind-ex}^{(2)} + E_{dis}^{(2)} + E_{dis-ex}^{(2)} \qquad (1)$$

1.5 Hirshfeld Analysis

Important intermolecular interactions within the crystal structure of PYDB-TCNB were identified through Hirshfeld surface analyses using Crystal Explorer 3.1.[7,8] The Hirshfeld surface is defined as the set of points in 3D space where the ratio of the pro molecule's electron density to the pro crystal's electron density is 0.5. The exploration of intermolecular contacts is provided by mapping normalised contact distances (d_{norm}), which is a function of the closest distance from the point to the nuclei interior (d_i) and exterior (d_e) to the surface, as well as on the van der Waals radii (r^{vdw}). 2D fingerprints were generated by deriving the Hirshfeld surface and plotting the fraction of surface points as a function of di and de, providing a visual summary of intermolecular contacts within the crystal.

1.6 Coulombic Coupling Calculation

Electronic energy transfer (EET) or resonance energy transfer (RET) refers to the process of energy transfer from a photoexcited donor molecule to a nearby ground-state acceptor molecule.[9,10] In Gaussian 16, the EET analysis employs a quantum mechanical model based on a DFT description of the wavefunction, incorporating a time-dependent variational approach. This involves performing an excited-state calculation for each fragment and then computing all couplings among the resulting states. For singlet excitation energy transfer (SEET), the electronic coupling comprises three terms,

$$V^{SEET} = V^{Coul} + V^{exch} + V^{ovlp} \quad (2)$$

Where, V^{Coul} is the Coulombic coupling between electronic transitions, V^{exch} is Dexter's exchange coupling and V^{ovlp} is the term used to describe the overlap of donor-acceptor orbitals.

$$V^{Coul} = \iint dr_1 dr_2 \frac{\rho_D^{tr*}(r_1)\rho_A^{tr}(r_2)}{|r_1 - r_2|} \quad (3)$$

Where, $\rho_D^{tr}(r_1)$ and $\rho_A^{tr}(r_2)$ are the transition densities (the diagonal element of the density matrix), respectively, of the donor and acceptor.

TD-DFT calculation was performed on **CD** after defining each carbazole dimer as a fragment (Figures S26 and S27) for the S_0 to $S_{3/5}$ transition at CAM-B3LYP-D3/def2-SVP, and Coulombic coupling between the states was procured.

1.7 Femtosecond Transient Absorption (fsTA) Measurement

A Spectra-Physics Mai Tai SP mode-locked laser, with an operating frequency of 86 MHz and emitting light at 800 nm, served as the seed for a Spectra-Physics Spitfire ace regenerative amplifier. The regenerative amplifier operated at a repetition rate of 1 kHz and produced an output energy of 5.5 mJ. A fraction of the amplified output was utilized to generate a 355 nm pump pulse through TOPAS. Simultaneously, the remaining 800-nm pulse was delayed in an ExciPro pump-probe spectrometer. A sapphire crystal introduced into this path generated a white light continuum, which was then split into two streams, serving as probe and reference pulses. Femtosecond transient absorption spectra of the

sample were captured using a dual diode array detector with a detection window of 200 nm and an optical delay of 3.6 ns. Sample solutions were housed in a rotating cuvette with a 1.2 mm path length for recording. To enable accurate deconvolution of the transient absorption data, an instrument response function (IRF) was determined. The IRF, established through a solvent (10% benzene in methanol) two-photon absorption, was approximately 110 fs at around 530 nm. An 80% neutral density filter regulated the incident flux on the sample. For the fsTA measurements, the samples were excited with a 200-nJ, 100-fs laser pulse. **CD** was excited at 355 nm.

1.8 Nanosecond Transient Absorption (nsTA) Measurement

Nanosecond laser flash photolysis measurements were carried out on nitrogen-purged solutions of **CD** in THF. These experiments employed an Applied Photophysics Model LKS-60 laser kinetic spectrometer, in which the second harmonic (532 nm, approximately 10 ns pulse duration) of a Quanta Ray INDI-40-10 series pulsed Nd:YAG laser served as the excitation source. The decay traces obtained from the nanosecond transient absorption (nsTA) kinetics experiment, specifically at a single wavelength (510 nm), were subjected to exponential fitting using OriginPro software.

1.8.1 Global Analysis

The fsTA spectra were analysed globally using Glotaran software.[11] This process involved assessing the instrument time response function and the group velocity dispersion of the white continuum, enabling the computation of decay time constants and dispersion-compensated spectra. In global analysis, all wavelengths were simultaneously scrutinised, utilising a sequential model to generate evolution-associated spectra (EAS).

The time-resolved spectroscopy data are measured as a function of the experimental spectral variable wavelength λ and the independent experimental variable time t relative to the instant of excitation. The model underlying the data matrix is a superposition of n_{comp} components given by the equation,

$$\Psi(\lambda, t) = \sum_{l=1}^{n_{comp}} c_l(t)\varepsilon_l(\lambda) \qquad (4)$$

where c_l and ε_l are the unknown concentration profile and spectrum of the component, respectively.

The first step in modelling these data typically involves looking at the singular value decomposition of the dataset. The singular value decomposition (SVD) is a matrix factorisation technique which can be used to explore the number of spectrally and temporally independent components in the data matrix which is an important aspect of defining an initial model (Golub GH, Van Loan CF, 1996, Matrix Computations. 3rd edition. The Johns Hopkins University Press, Baltimore).

Upon fitting the fsTA data with a sequential model in Glotaran, we get the SVD of the residual matrix, the estimated kinetic parameters, the spectra (EAS), the normalised spectra, and the concentration profiles in an interactive user platform. In a sequential or unbranched unidirectional model, the associated spectra are called evolution-associated spectra (EAS), and the model of equation 3 then reads as,

$$\Psi(\lambda, t) = \sum_{l=1}^{n_{comp}} c_l^{EAS}(t, \theta)EAS_l(\lambda) \qquad (5)$$

As lifetimes increase, the EAS visualises the spectral evolution. It is crucial to note that EAS illustrates the temporal evolution of spectra and may not necessarily represent any physical or chemical species. Instead, EAS signifies spectral changes and their corresponding time constants.

1.9 Triplet Quantum Yield (ϕ_T) Measurements

To estimate the triplet quantum yield (ϕ_T) of **CD**, the process of triplet energy transfer to β-carotene was used with $[Ru(bpy)_3]^{2+}$ as the reference ($\phi_T \sim 1$) as reported in the literature.[12] A known, equal volume of β-carotene in $CHCl_3$ was added to the optically matched solutions (0.1–0.2 absorbance at 532 nm) of $[Ru(bpy)_3]^{2+}$ in CH_3OH and **CD** in THF solvents. The energy transfer from $[Ru(bpy)_3]^{2+}$ or **CD** populates the β-carotene triplet, which is monitored at 530 nm. The ϕ_T values of **CD** were calculated according to the following equation, where superscripts "Sam" and "Ref" refer to the sample **CD** and reference $[Ru(bpy)_3]^{2+}$, respectively. k_{obs} is the pseudo-first-order rate constant for the growth of the β-carotene triplet, and k_0 is the rate constant for the decay of the donor triplets (in the absence of β-carotene) in solutions that contained $[Ru(bpy)_3]^{2+}$ or **CD** with the same absorbance.

$$\phi_T^{Sam} = \phi_T^{Ref} \times \frac{\Delta A^{Sam}}{\Delta A^{Ref}} \times \frac{k_{obs}^{Sam}}{k_{obs}^{Sam} - k_0^{Sam}} \times \frac{k_{obs}^{Ref} - k_0^{Ref}}{k_{obs}^{Ref}} \qquad (6)$$

1.10 Huang-Rhys Factor (S)

The Huang–Rhys factor is a dimensionless parameter that quantifies the strength of exciton–phonon (vibronic) coupling in an electronic transition. It represents the average number of vibrational quanta coupled to the excitation and governs the intensity distribution of vibronic peaks according to $\boldsymbol{I_{(0-n)} \propto (S^n/n!)e^{(-S)}}$. In practice, it is often approximated from emission spectra as $\boldsymbol{S \approx I_{(0-1)}/I_{(0-0)}}$. A small S value indicates weak coupling with dominant 0–0 emission, while larger S values correspond to stronger coupling and more pronounced vibronic sidebands, reflecting increased interaction between the exciton and molecular vibrations.

1.11 Reorganisation energy (λ) for Huang–Rhys factor

The reorganisation energy is the energy required for nuclear relaxation between ground and excited-state configurations during an electronic transition, and it directly reflects the extent of structural distortion induced by excitation. It is related to the Huang–Rhys factor through $\boldsymbol{\lambda = S\,\hbar\omega}$, where $\hbar\omega$ is the vibrational mode energy, and can also be estimated from the Stokes shift using $\boldsymbol{\lambda = \Delta E_{(Stokes)}/2}$. A higher λ value indicates stronger exciton–phonon coupling, leading to greater geometric reorganisation, broader spectral features, and increased energy dissipation into vibrational modes, whereas a smaller λ value indicates more rigid systems with weaker coupling

1.12 Reorganization Energy (ΔE_{reorg})

The reorganization energy (ΔE_{reorg}) quantifies the structural relaxation accompanying an electronic transition and reflects the extent of geometric distortion between the initial and final electronic states. It is commonly employed to evaluate the coupling between electronic and nuclear motions, where larger ΔE_{reorg} values indicate greater structural reorganization upon excitation or emission.

To further assess structural variations, the root-mean-square deviation (RMSD) between the optimized geometries was calculated. RMSD provides a quantitative measure of the overall geometric displacement between two molecular structures after optimal alignment, with smaller values indicating higher structural similarity.

In the present study, both ΔE_{reorg} and RMSD were computed for the carbazole dimer at 298 and 77 K to evaluate the extent of temperature-dependent structural reorganization and its possible influence on the observed photophysical properties.

The reorganization energy (ΔE_{reorg}) was calculated using the four-point method according to

$$\Delta E_{reorg} = \lambda = \lambda_{GS} + \lambda_{ES}$$

where

$\lambda_{GS} = E(S_0,T_1) - E(S_0,S_0)$

$\lambda_{ES} = E(T_1,S_0) - E(T_1,T_1)$

Thus,

$\Delta E_{reorg} = [E(S_0,T_1) - E(S_0,S_0)] + [E(T_1,S_0) - E(T_1,T_1)]$

where E(A,B) denotes the energy of electronic state A evaluated at the optimized geometry of state B. $E(S_0,S_0)$ and $E(T_1,T_1)$ correspond to the energies of the optimized ground-state and triplet-state geometries, respectively.

Root-Mean-Square Deviation (RMSD)

The structural deviation between the optimized geometries was quantified using the root-mean-square deviation (RMSD):

$$RMSD = \sqrt{[(1/N)\ \Sigma i=1N\ |ri(1) - ri(2)|^2]}$$

where N is the number of atoms, and ri(1) and ri(2) are the Cartesian coordinates of atom i in the two aligned structures. Lower RMSD values indicate greater structural similarity and, therefore, smaller geometric changes upon electronic excitation.

Section 2: Syntheses and Characterisation

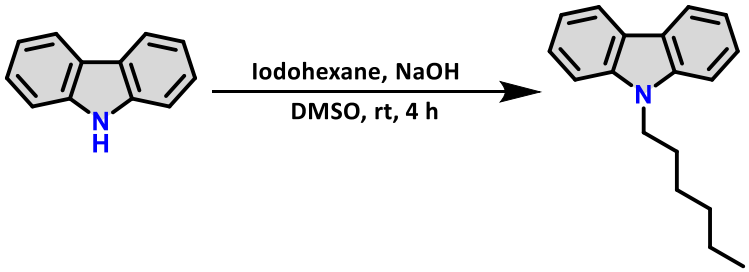

Scheme S1: Synthesis of 9-hexyl-9H-carbazole

Procedure 1: 500 mg (2.99 mmol, 1eq) of 9-H carbazole was dissolved in 10 mL DMSO in a double-neck RB flask. Stir it till carbazole is completely dissolved. Add 2 ml more of DMSO. Then add 10 ml 10% solution of NaOH and 1 ml of 1-bromohexane (7.2 mmol, 1.2eq). Stir the reaction at room temperature for 4 hours. The organic layer was separated and concentrated. The product was purified using column chromatography (petroleum ether) to afford a white powder. (2.7 mmol, 90% yield.)

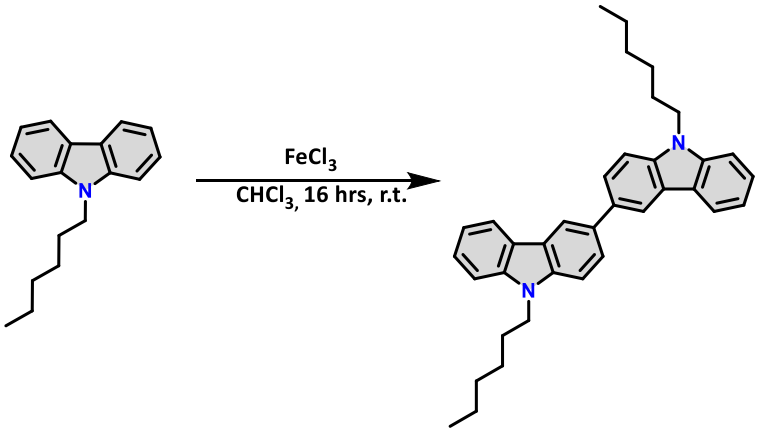

Scheme 2: Synthesis of 9,9'-dihexyl-9H,9'H-3,3'-bicarbazole (**C-CD**)

Procedure 2: To a stirred solution of 500 mg of N-hexyl carbazole (1.99 mmol, 1eq) in 20 ml dry, distilled chloroform under Argon atmosphere, 484.31 mg of $FeCl_3$ (2.98 mmol, 1.5eq) was added. The reaction was stirred at room temperature for 16 hours. After the reaction, water was added to the mixture, and the organic layer was separated, concentrated and purified by column chromatography (pet ether: DCM 1:99), to afford a white gel-like product. (0.796 mmol, 40% yield).

1H NMR (500 MHz, Chloroform-*d*) : δ 8.34 (s, 2H), 8.12 (d, *J* = 7.7 Hz, 2H), 7.76 (d, *J* = 8.5 Hz, 2H), 7.50 – 7.40 (m, 4H), 7.42 – 7.28 (m, 4H), 4.28 (t, *J* = 7.4 Hz, 4H), 1.85 (t, *J* = 7.6 Hz, 4H), 1.33 – 1.21 (m, 12H), 0.82 (d, *J* = 7.1 Hz, 6

Section 3: Tables

Table S1: Crystallographic data and refinement parameters of **CD**.

Parameters	CD
Formula	C_{36} H_{40} N_2
Formula weight	500.32
Crystal system	monoclinic
Space group, Z	P_{21}/c
a, Å	9.10
b, Å	13.85
c, Å	11.07
α, deg	90
β, deg	98.71
γ, deg	90.00
V, Å^3	1380.07
R-factor (%)	3.96

Table S2: Unit cell parameters of the crystal at 298 K and 77 K, respectively

Space group	$P2_1/c$
Cell lengths	a = 9.50 Å b = 13.73 Å c = 11.12 Å
Cell angles	α = 90.00° β = 97.90° γ = 90.00°
Cell volume	1437.21 Å³
R-factor	4.67 %
CCDC number	2561138

Space group	$P2_1/c$
Cell lengths	a = 9.10 Å b = 13.85 Å c = 11.07 Å
Cell angles	α = 90.00° β = 98.71° γ = 90.00°
Cell volume	1380.07 Å³
R-factor	3.96 %
CCDC number	2546883

Table S3: Unit cell parameters of the crystal at 100 K, 150 K, 200 K, 250 K and 300 K, respectively.

Parameters	**100 K**	**150 K**	**200 K**	**250 K**	**300 K**
a (Å)	9.0952	9.1578	9.2284	9.3187	9.4303
b (Å)	13.8539	13.8431	13.8268	13.8006	13.7566
c (Å)	11.0816	11.0945	11.1075	11.1213	11.1339
α (º)	90	90	90	90	90
β (º)	98.743	98.557	98.359	98.146	97.933
γ (º)	90	90	90	90	90
Volume	1380	1390	1402	1415	1430

Table S4: Interaction energies in selected dimers determined by SAPT(0)/6-311G+(d,p) calculations and SAPT(0) energy components for **CD**

Dimer	**Electrostatic KJ/mol**	**Exchange KJ/mol**	**Induction KJ/mol**	**Dispersion KJ/mol**	**Total Energy KJ/mol**
1	-15.847	37.161	-4.857	-78.237	-61.780
2	-2.809	7.334	-0.554	-11.128	-7.158

Table S5: Relative % intermolecular interactions obtained from Hirshfeld analysis of **CD**

Interaction	**%N•••N**	**%N•••C**	**%N•••H**	**%C•••C**	**%C•••H**	**%H•••H**
	0.1	0.1	0.9	0.1	32.9	65.9

Table S6: Absorption maxima, emission maxima, fluorescence quantum yield and lifetime of **CD**

Solvents	**CD**			
	λ_{Abs} (nm)	λ_{Emi} (nm)	Φ_f (%)	τ_F (ns)
Tetrahydrofuran	300	407	25.09	0.43
				4.12
Acetonitrile	299	408	4.06	1.11
				6.04

Reference: Quinine sulphate in 0.5 M H_2SO_4

Table S7: TD-DFT Vertical excitation energies of singlets and triplets of **CD** computed at CAM-B3LYP-D3/def2-SVP level of theory in monomer state in vacuum.

Singlet State	Energy (eV)	Oscillator Strength (f)	Triplet State	Energy (eV)
S_1	3.80	0	T_1	3.15
S_2	4.10	0.07	T_2	3.19
S_3	4.27	0.62	T_3	3.43
S_4	4.58	0	T_4	3.51
S_5	4.60	1.41	T_5	3.67
S_6	5.02	0	T_6	3.97
S_7	5.04	0	T_7	4.14
S_8	5.18	0.03	T_8	4.44
S_9	5.24	0	T_9	4.51
S_{10}	5.30	0.20	T_{10}	4.56
S_{11}	5.33	0.11	T_{11}	4.589
S_{12}	5.39	0.004	T_{12}	4.59
S_{13}	5.45	0	T_{13}	4.789
S_{14}	5.56	0.36	T_{14}	4.79
S_{15}	5.61	0	T_{15}	5.01

Table S8: TD-DFT Vertical excitation energies of singlets and triplets of dimeric arrangement **CD@298 K** computed at CAM-B3LYP-D3/def2-SVP level of theory at room temperature (298 K) in dimeric state.

Singlet State	Energy (eV)	Oscillator Strength (f)	Triplet State	Energy (eV)
S_1	3.7701	0.0017	T_1	2.8012
S_2	3.8782	0.000	T_2	2.8320
S_3	4.1724	0.1143	T_3	2.8926
S_4	4.2001	0.0001	T_4	3.0812
S_5	4.2154	1.5999	T_5	3.1027
S_6	4.2623	0.0001	T_6	3.2113
S_7	4.5496	0.000	T_7	3.3155
S_8	4.5755	0.6542	T_8	3.4184
S_9	4.5911	0.0001	T_9	3.5654

S_{10}	4.5999	0.0001	T_{10}	3.6656
S_{11}	4..8013	0.0080	T_{11}	3.9520
S_{12}	4.8171	0.000	T_{12}	3.9574
S_{13}	4..8475	0.000	T_{13}	4.1255
S_{14}	4.8587	0.000	T_{14}	4.1344
S_{15}	4.992	0.000	T_{15}	4.4299

Table S9: TD-DFT Vertical excitation energies of singlets and triplets of dimeric arrangement **CD@77 K** computed at CAM-B3LYP-D3/def2-SVP level of theory at low temperature (77 K) in dimeric state.

Singlet State	**Energy (eV)**	**Oscillator Strength (f)**	**Triplet State**	**Energy (eV)**
S_1	3.7711	0.001	T_1	3.1514
S_2	3.7832	0.000	T_2	3.1623
S_3	4.0811	0.110	T_3	3.1843
S_4	4.0843	0.000	T_4	3.1944
S_5	4.2364	1.500	T_5	3.4154
S_6	4.2812	0.000	T_6	3.4223
S_7	4.5634	0.000	T_7	3.5321
S_8	4.5956	0.700	T_8	3.5311
S_9	4.6165	1.890	T_9	3.6793
S_{10}	4.6266	0.000	T_{10}	3.6797
S_{11}	4.8534	0.000	T_{11}	3.9811
S_{12}	4.8667	0.008	T_{12}	3.9861
S_{13}	4.9655	0.017	T_{13}	4.1548
S_{14}	4.9712	0.000	T_{14}	4.1635
S_{15}	5.0101	0.000	T_{15}	4.4518

Table S10: Coulombic coupling calculation employed using the EET method in the dimeric arrangement **CD@77 K** and **CD@298 K** computed at the CAM-B3LYP-D3/def2-SVP level of theory.

Room Temperature		
Energy Level	**Oscillator Strength**	**Total Coupling (cm^{-1})**
S_5	1.60	273.97
Low Temperature		
Energy Level	**Oscillator Strength**	**Total Coupling (cm^{-1})**
S_5	1.50	237.45

Table S11: Reorganization energy and root-mean square deviation (RMSD) of CD at 298 K and 77 K

	298 K	**77 K**
Reorganization energy (eV)	3.80	3.93
RMSD (Å)	3.15	3.16

Section 4: Schemes

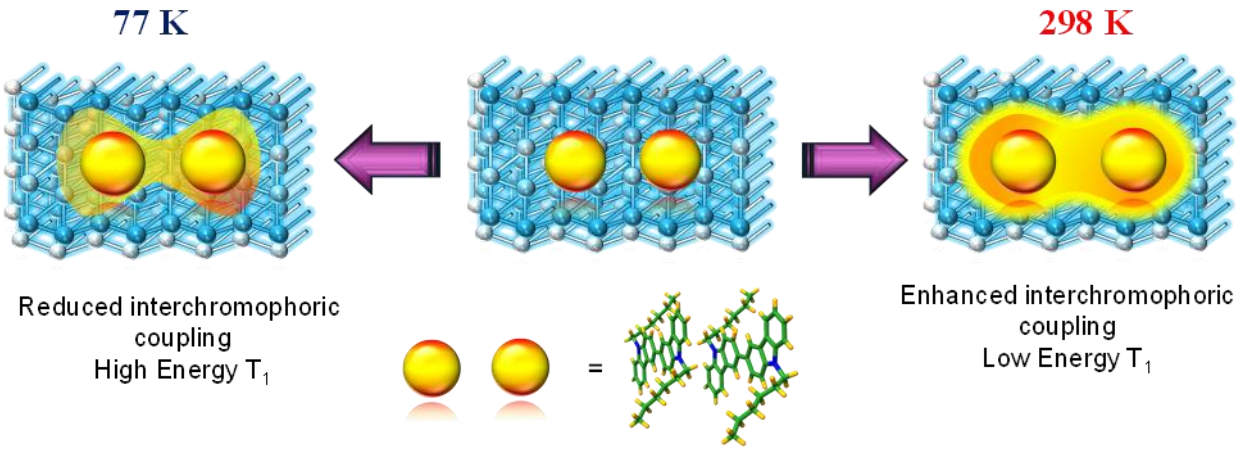

Scheme 1: Schematic illustration of interchromophoric excitonic coupling modulating the triplet state energy.

Section 5: Figures

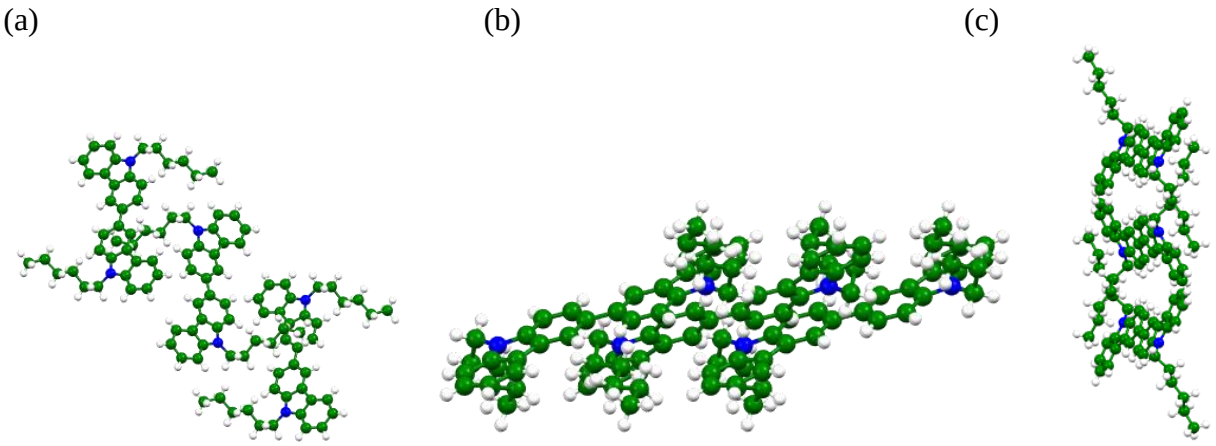

Figure S1. Crystal packing of **C-CD** viewed along (a) a-axis, (b) b-axis, and (c) c-axis, respectively.

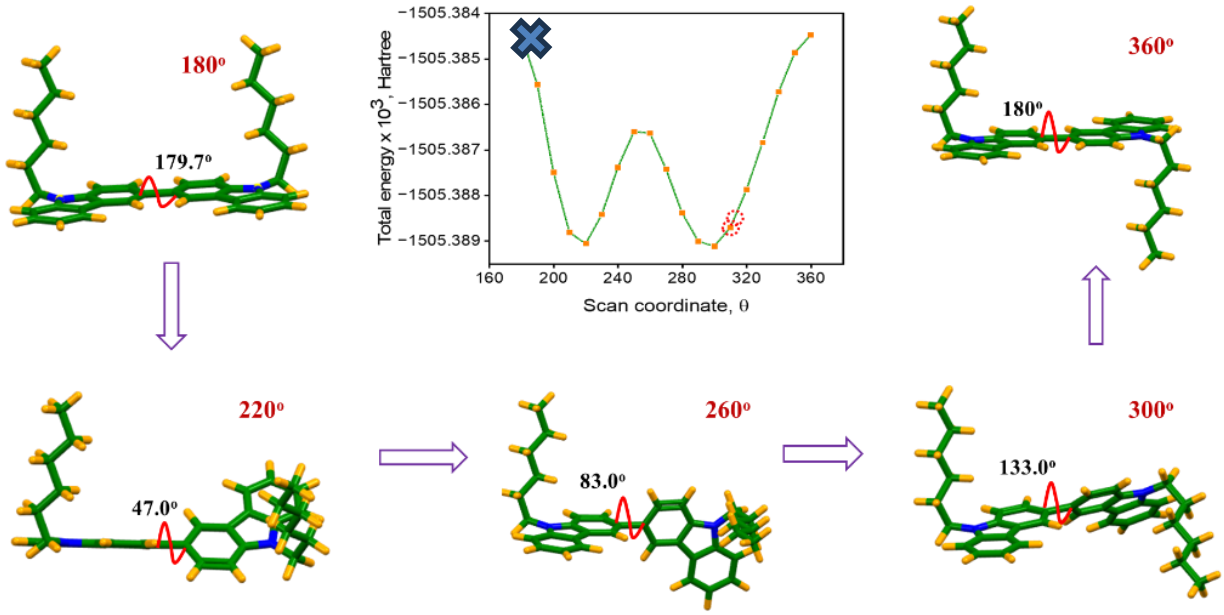

Figure S2: Potential Energy Surface Scan of **CD**, by changing the dihedral angle between two carbazole units (The cross mark indicates the dihedral angle between the C-C rotational offset in the CD crystal packing, which is 180 °).

(a) (b)

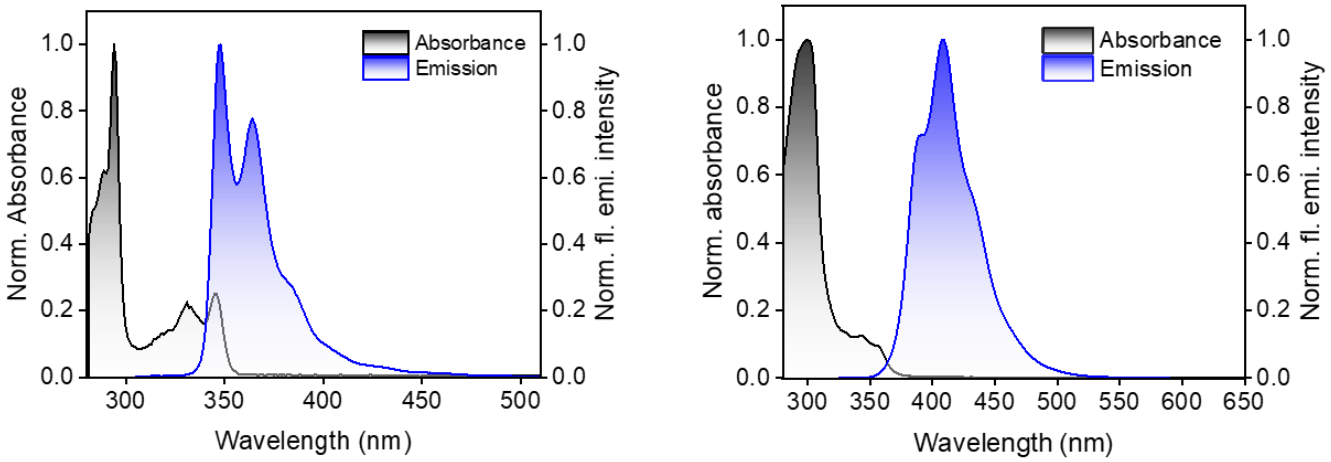

Figure S3: Co-plots of (a) absorbance and (b) emission of Cz-monomer and **CD** in THF.

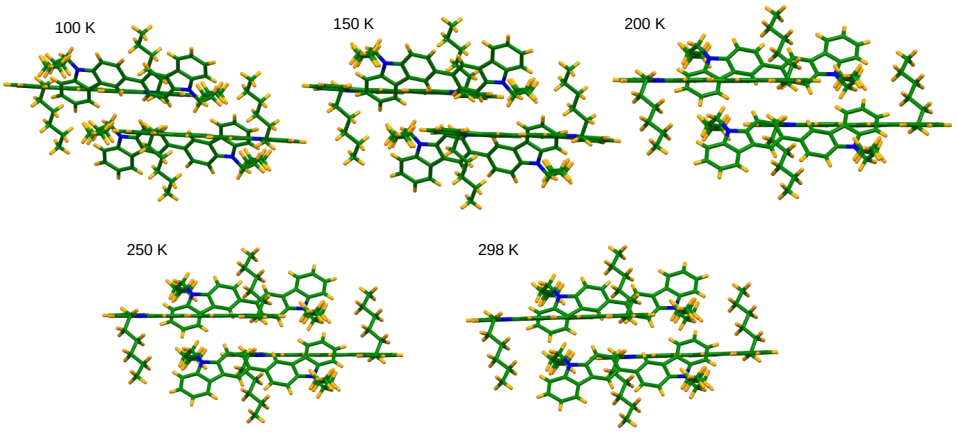

Figure S4: Packing arrangement of CD at 100 K, 150 K, 200 K, 250 K and 300 K.

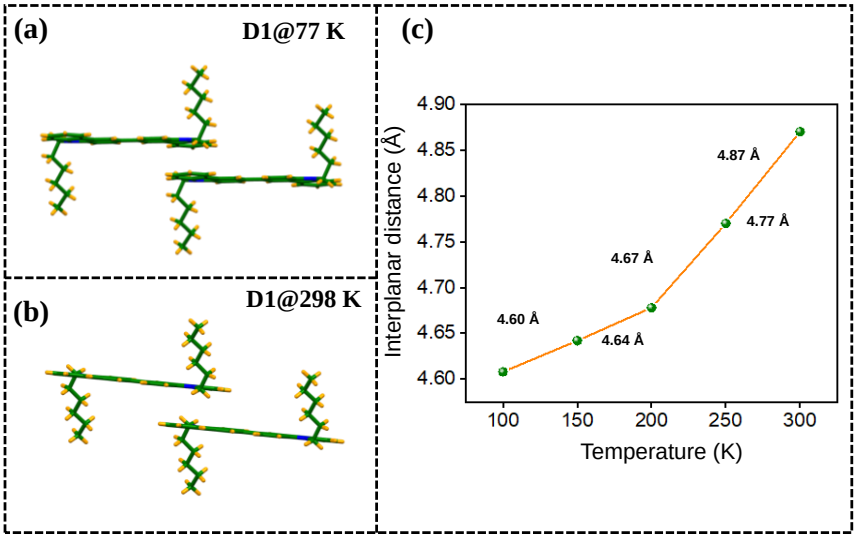

Figure S5: Isolated parallel dimer (D1) from Crystal packing of **CD** (a) 77 K, (b) 298 K and (c) Plot of Interplanar distance vs Temperature for D1

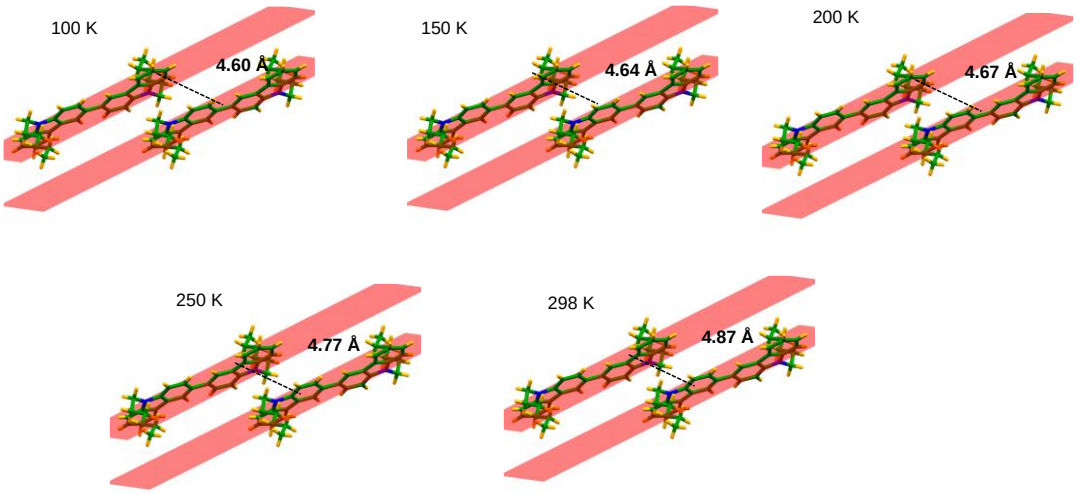

Figure S6: Interplanar distance of CD crystal packing at temperatures 100 K, 150 K, 200 K, 250 K and 300 K.

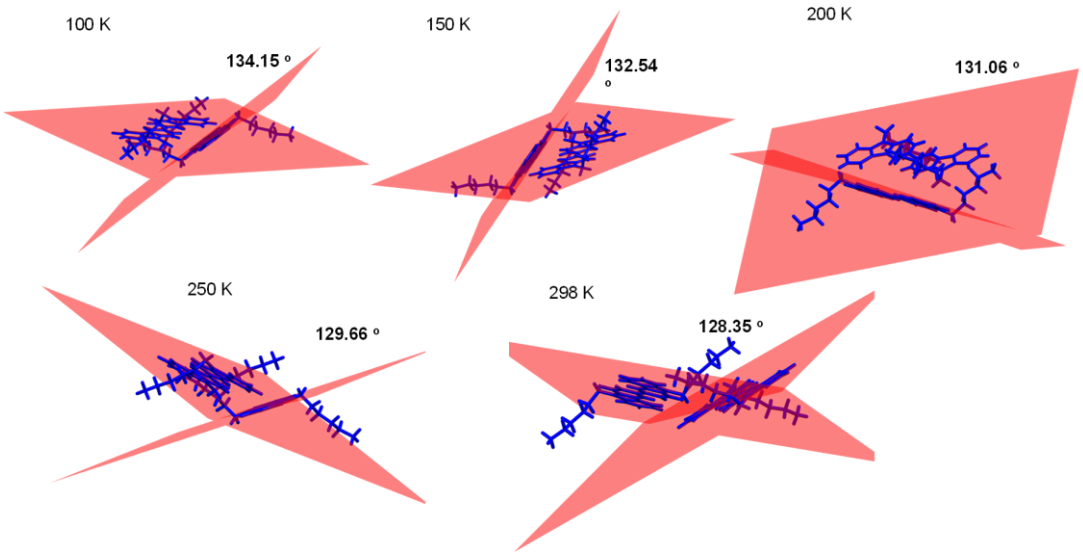

Figure S7: Interplanar angles of CD crystal packing at temperatures 100 K, 150 K, 200 K, 250 K and 300 K.

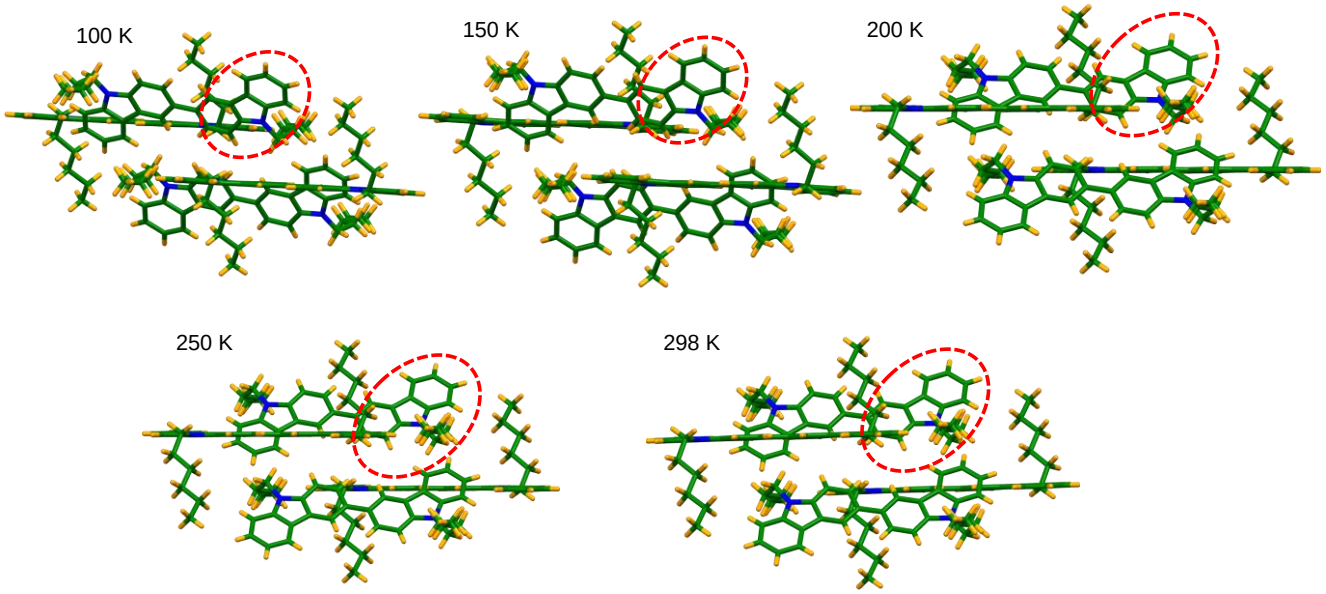

Figure S8: The crystallographic packing of **CD,** indicating the rotation of one **CD** molecule relative to the neighbouring **CD** molecule at different temperatures.

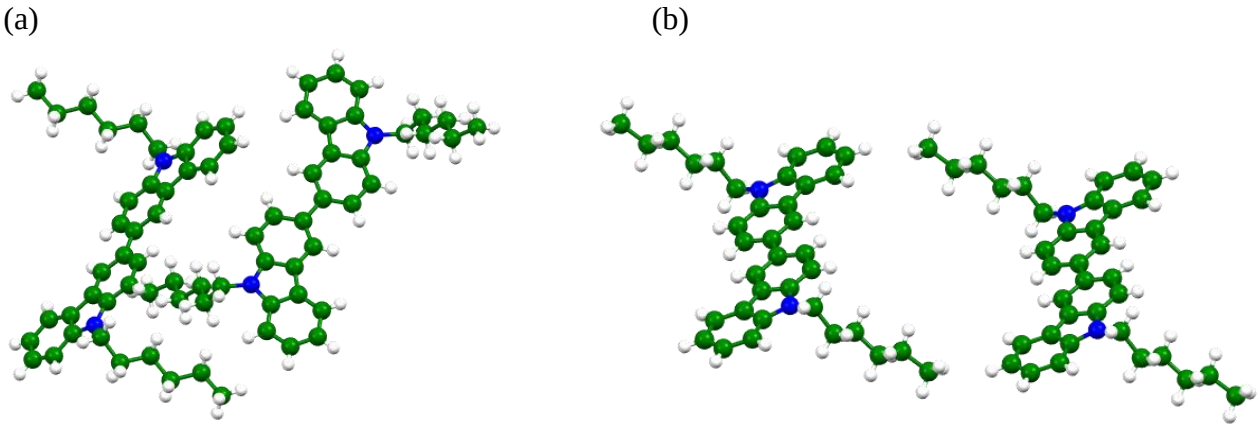

Figure S9: Dimers, (a) Dimer 1 and (b) Dimer 2, picked from the crystal packing at 298 K of **CD** for SAPT analysis.

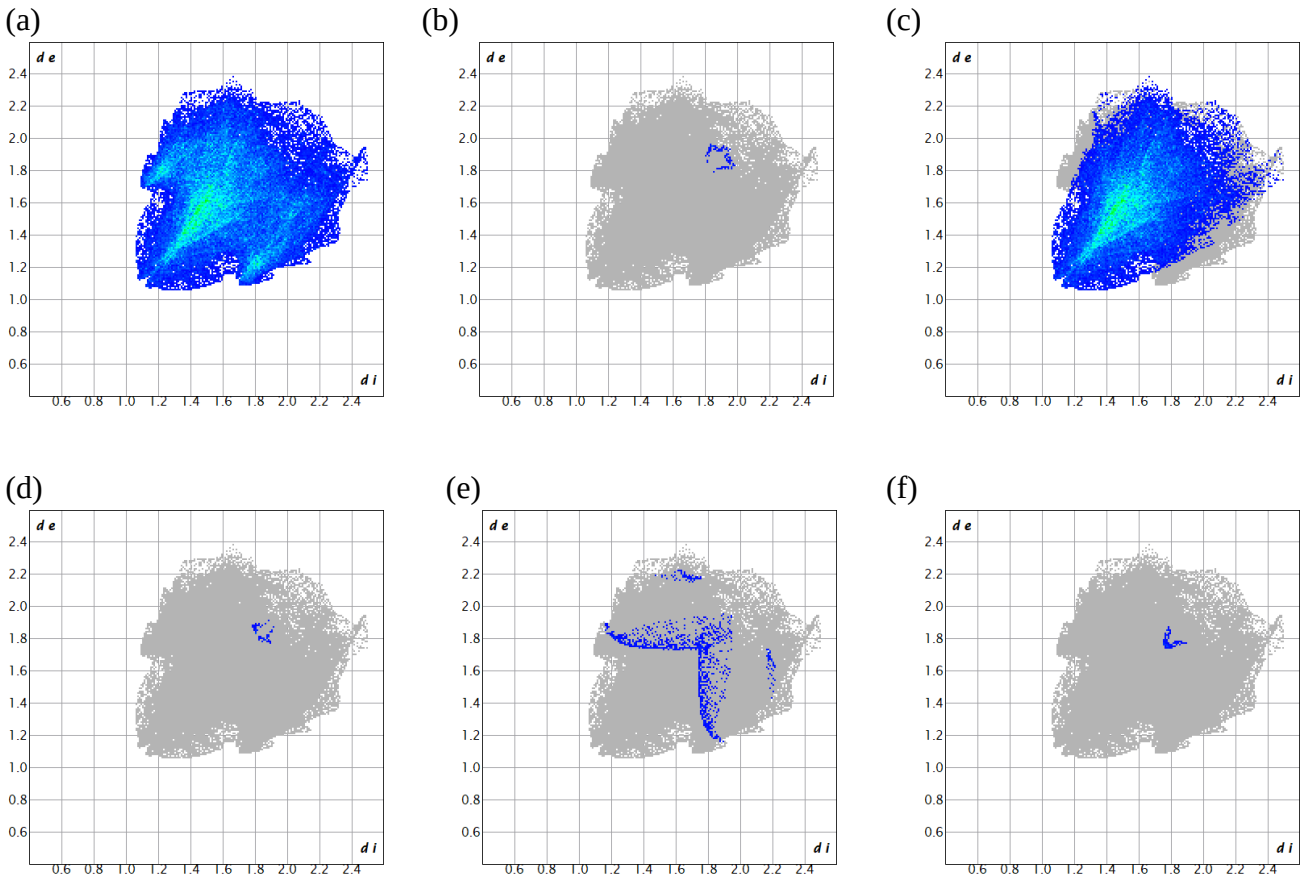

Figure S10: Hirshfeld surface analysis of **CD** showing (a) all surface interactions, (b) C-C interactions, (c) H-H interactions, (d) N-C interactions, (e) N-H interactions, and (f) N-N interactions.

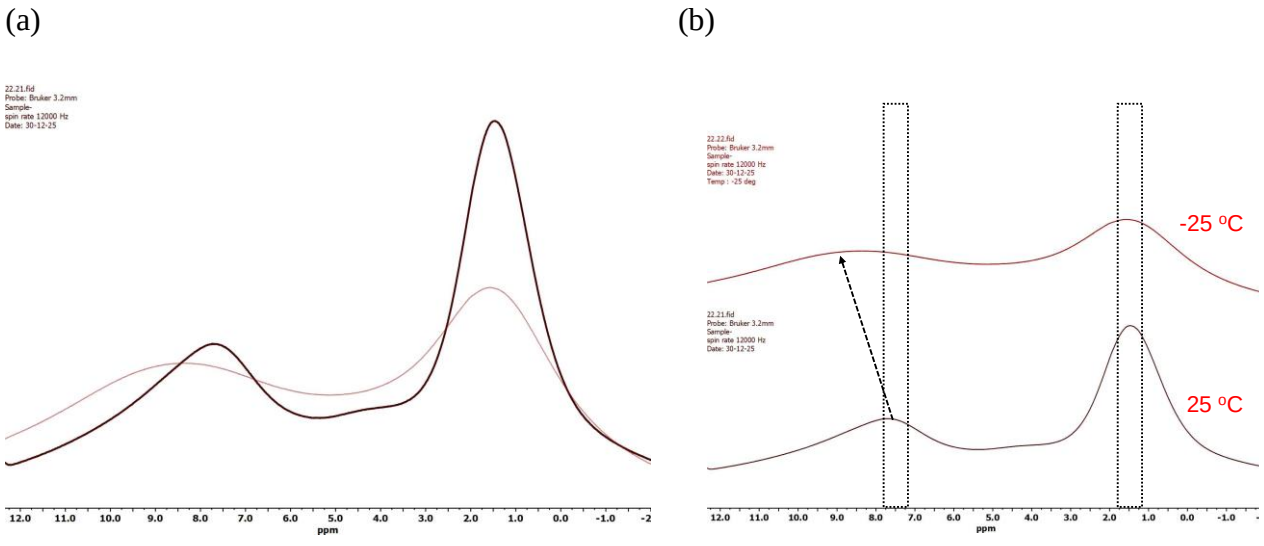

Figure S11: (a) Overlapped ^{1}H-NMR spectra of **CD** in the solid state at 248 K and 298 K, (b) ^{1}H-NMR spectra of **CD** at 248 K showing a downfield shift.

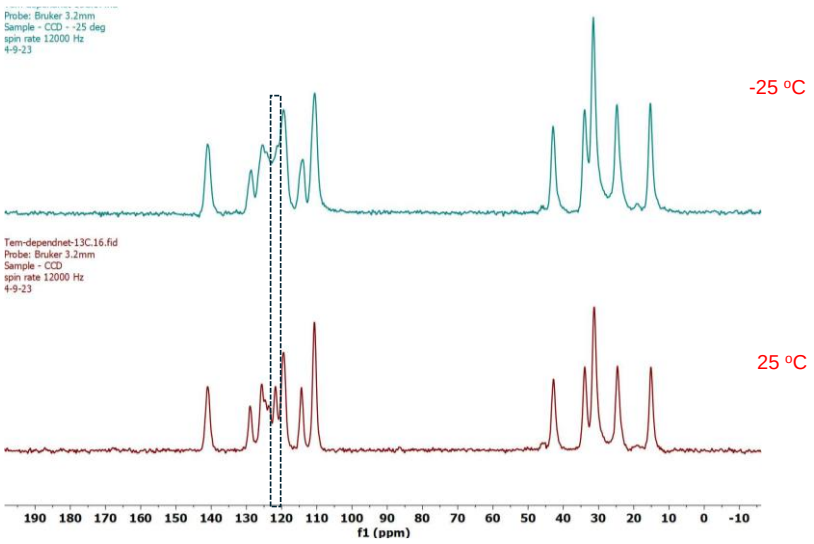

Figure S12: ^{13}C-NMR spectra of **CD** at 248 K and 298 K.

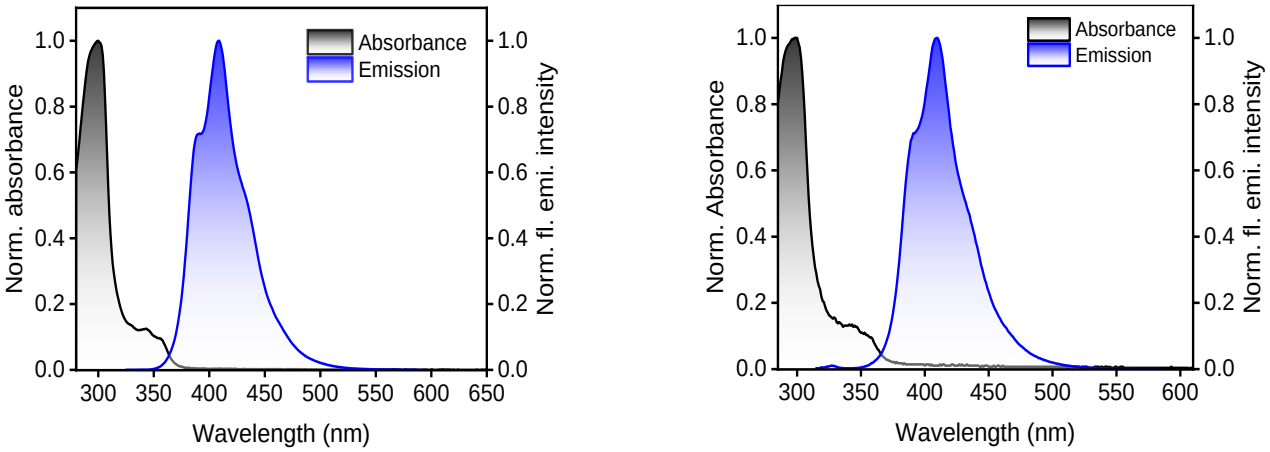

Figure S13: Steady-state absorption and emission spectra of **CD** in tetrahydrofuran (THF) and acetonitrile (ACN), respectively.

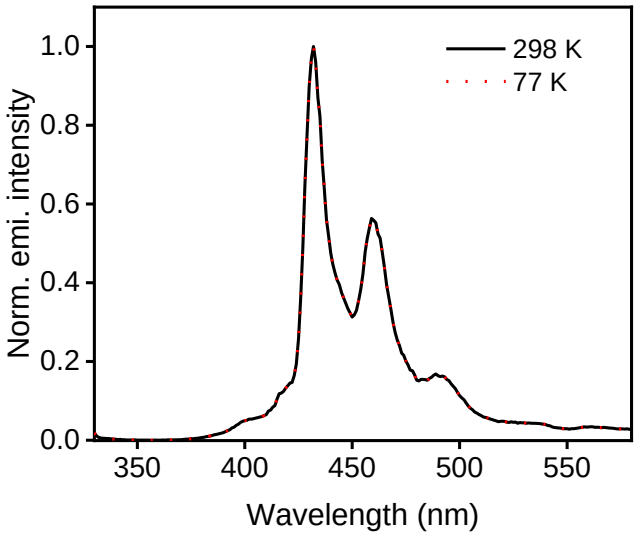

Figure S14: Prompt emission measurements of CD at 298 K and 77 K

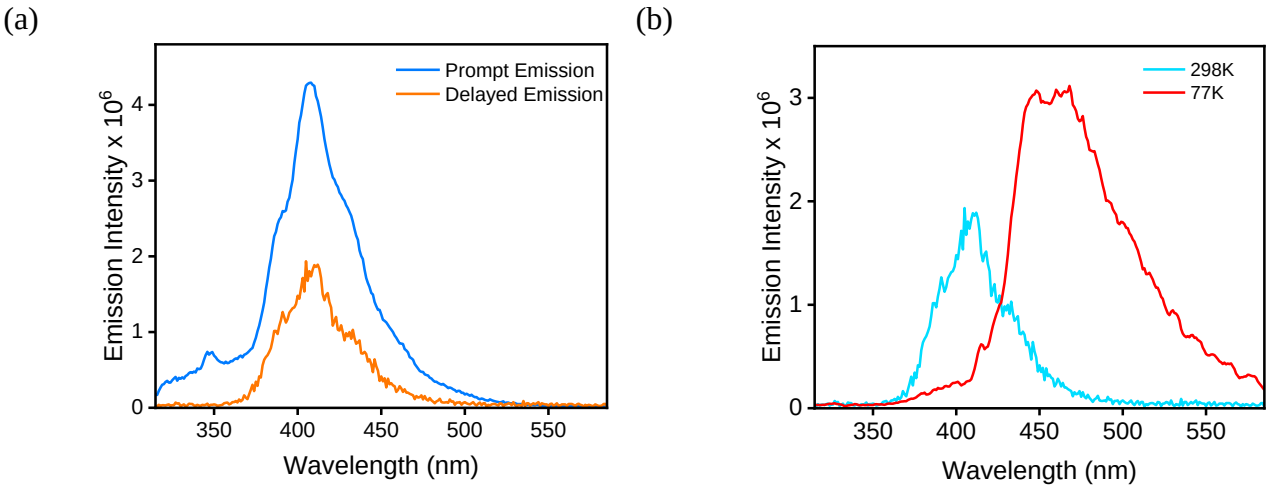

Figure S15: (a) Prompt emission and delayed emission of **CD** in THF and (b) delayed emission measurements at 298 K and 77 K.

(a) (b)

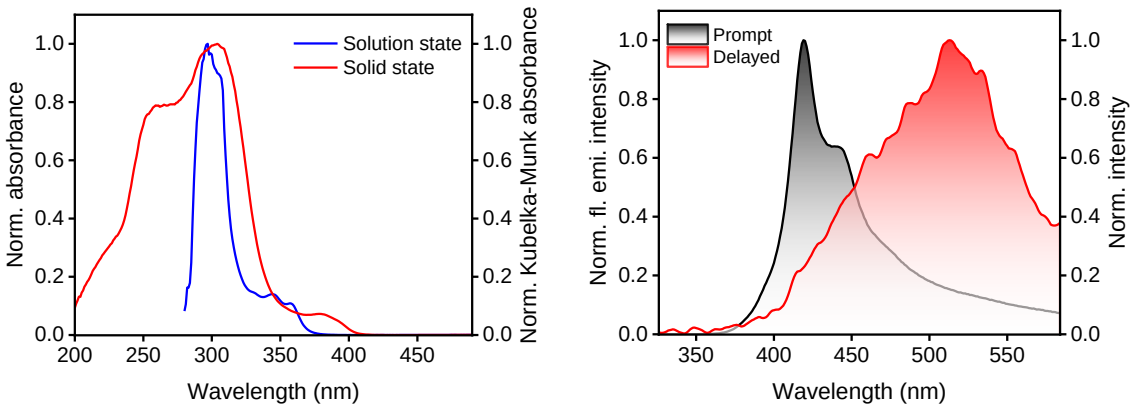

Figure S16: (a) Absorption spectra of CD in solution and solid state, and (b) prompt and delayed emission of CD in crystalline state.

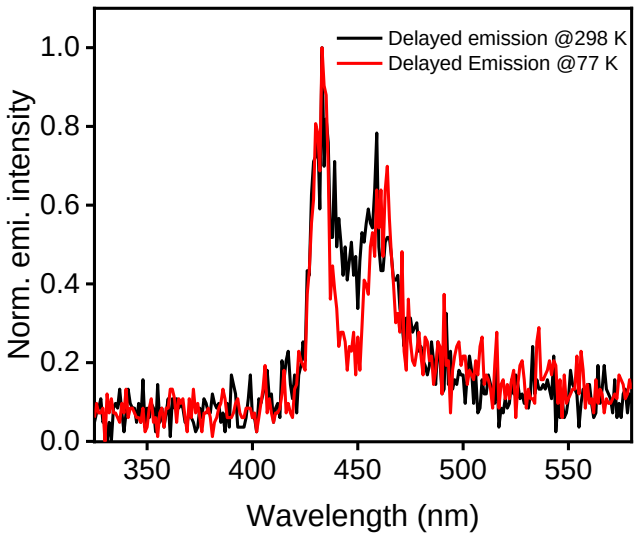

Figure S17: Delayed emission measurements of CD in the amorphous state at 298 K and 77 K.

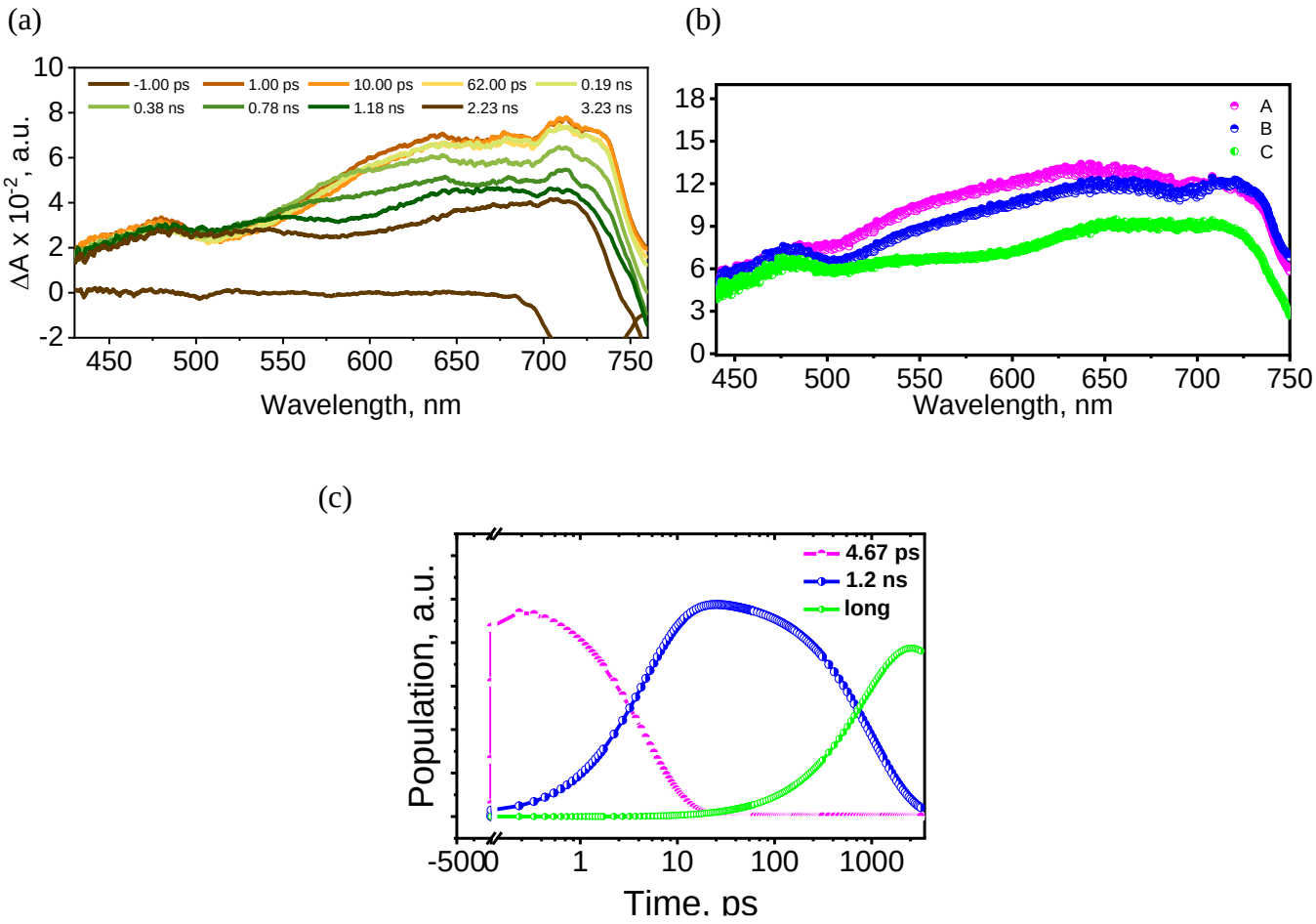

Figure S18: (a) The fsTA spectra of **CD** in Acetonitrile (ACN) showing the excited-state dynamics upon photoexcitation, (b) EAS reconstructed from global analysis of the fsTA data with the A → B →C→ GS kinetic model. (c) Relative population profile of the excited states fitted using the above kinetic models.

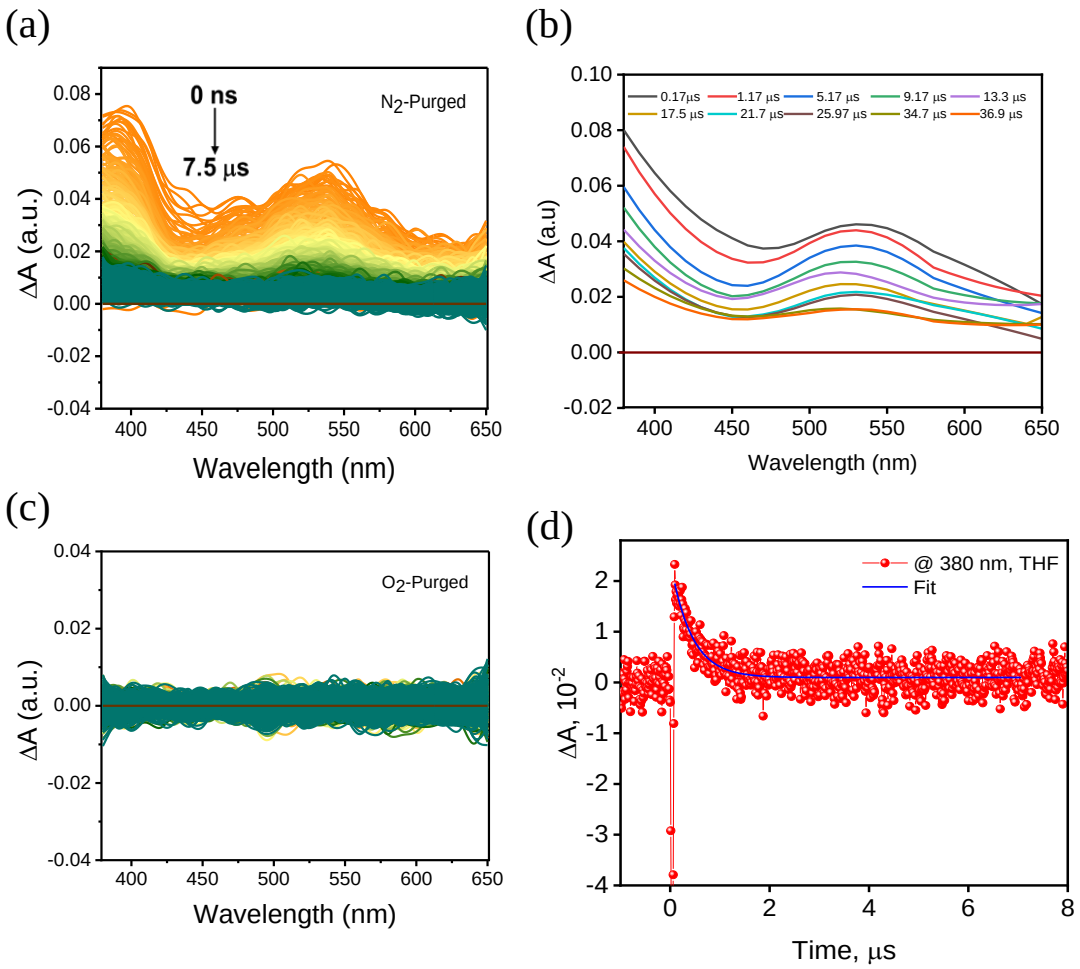

Figure S19: (a) Nanosecond transient absorption spectra of **CD** in ACN in N_2 purged solution. (b) EAS nsTA spectra at different times, (c) nsTA spectrum of **CD** in ACN after O_2 purging, and (d) fitting of nsTA spectra at 380 nm wavelength

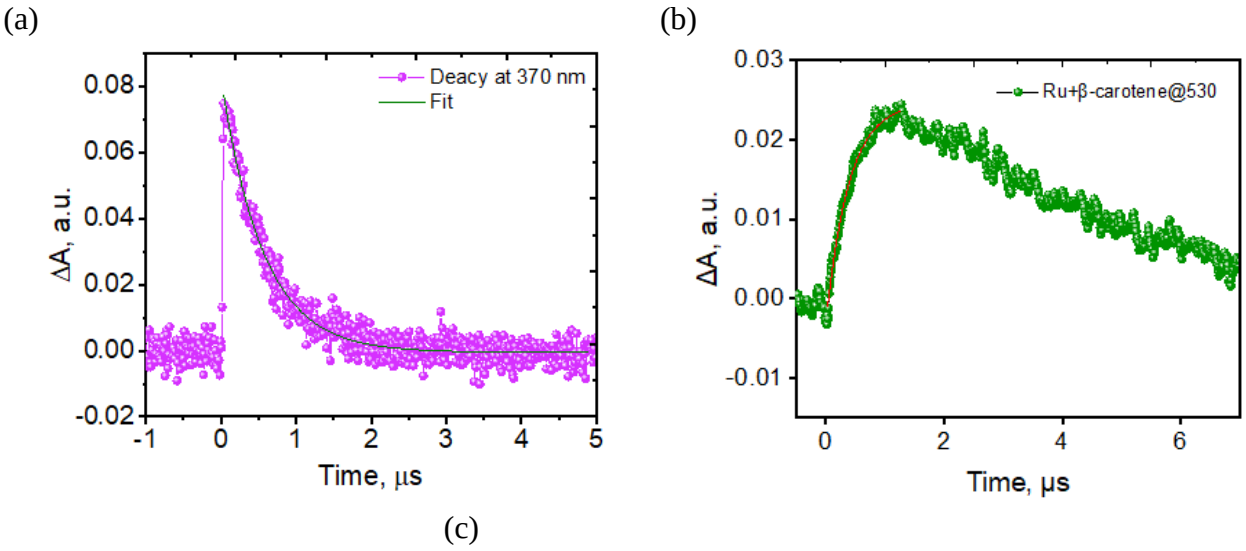

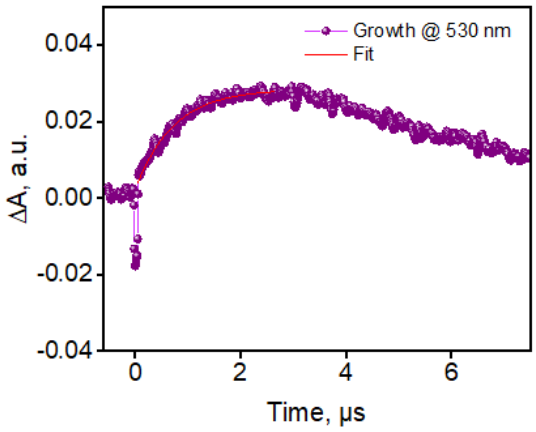

Figure S20: a) Nanosecond transient kinetic decay of $[Ru(bpy)_3]^{2+}$ at 370 nm. b) The growth profile of ^{3}βcarotene* formed in the mixture of $[Ru(bpy)_3]^{2+}$ and β-carotene in THF at 530 nm confirming the triplet–triplet energy transfer from $[Ru(bpy)_3]^{2+}$ to β-carotene. c) The growth profile of ^{3}β-carotene* formed in the mixture of **CD** and β-carotene, confirming the triplet-triplet energy transfer from **CD** to β-carotene in THF.

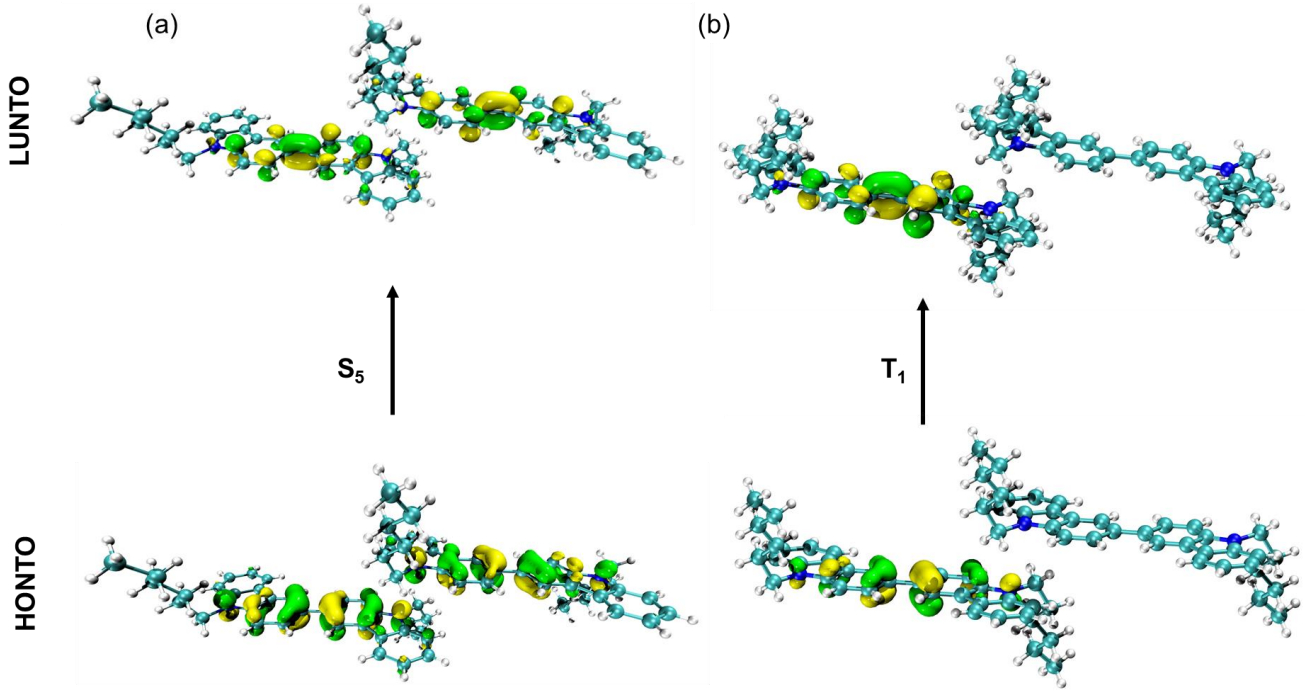

Figure S21: NTO analysis for S_5 and T_1 states.

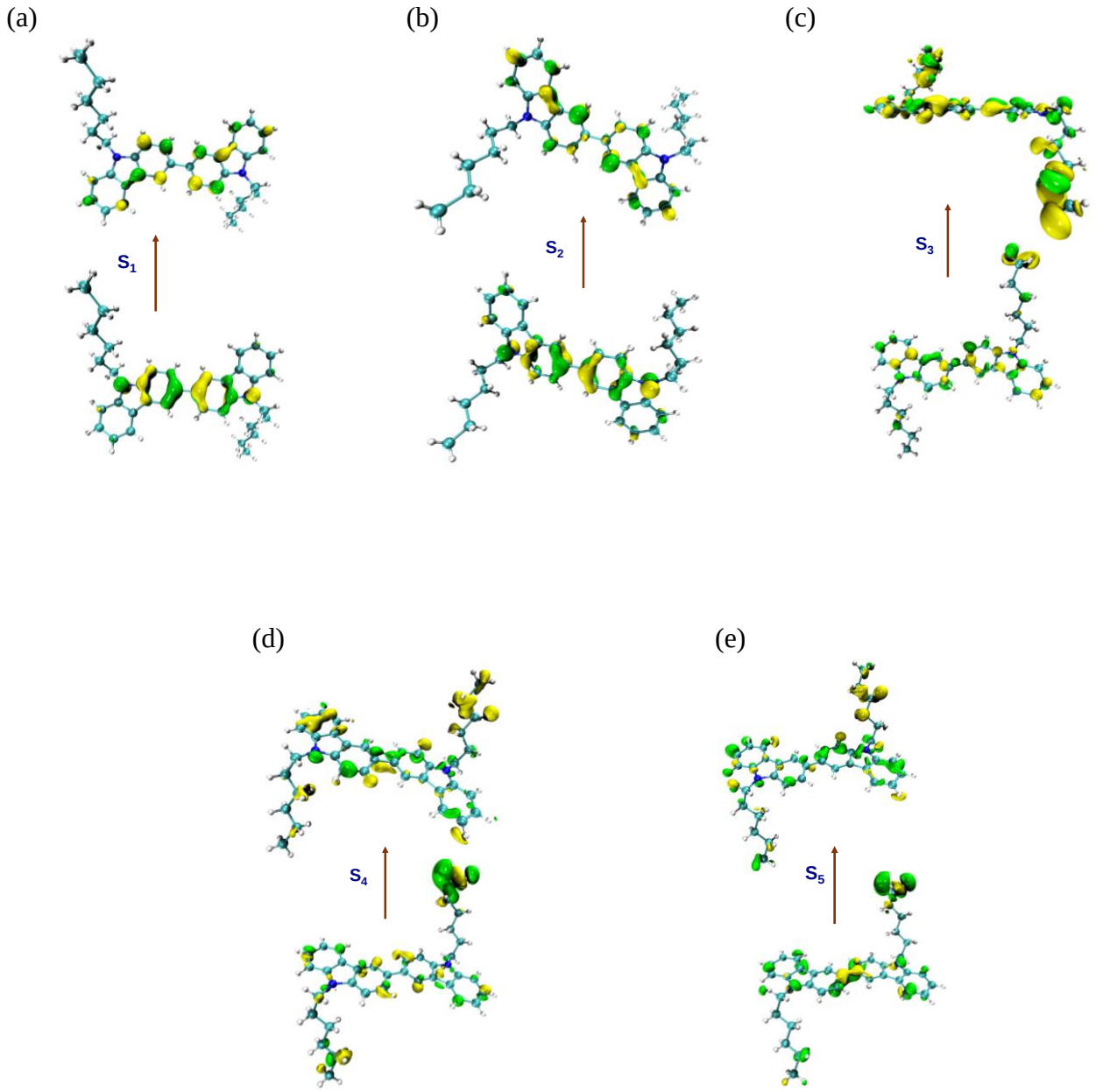

Figure S22: Natural Transition Orbital (NTO) analysis of (a) S_1 state, (b) S_2 state, (c) S_3 state, (d) S_4 state and (e) S_5 state.

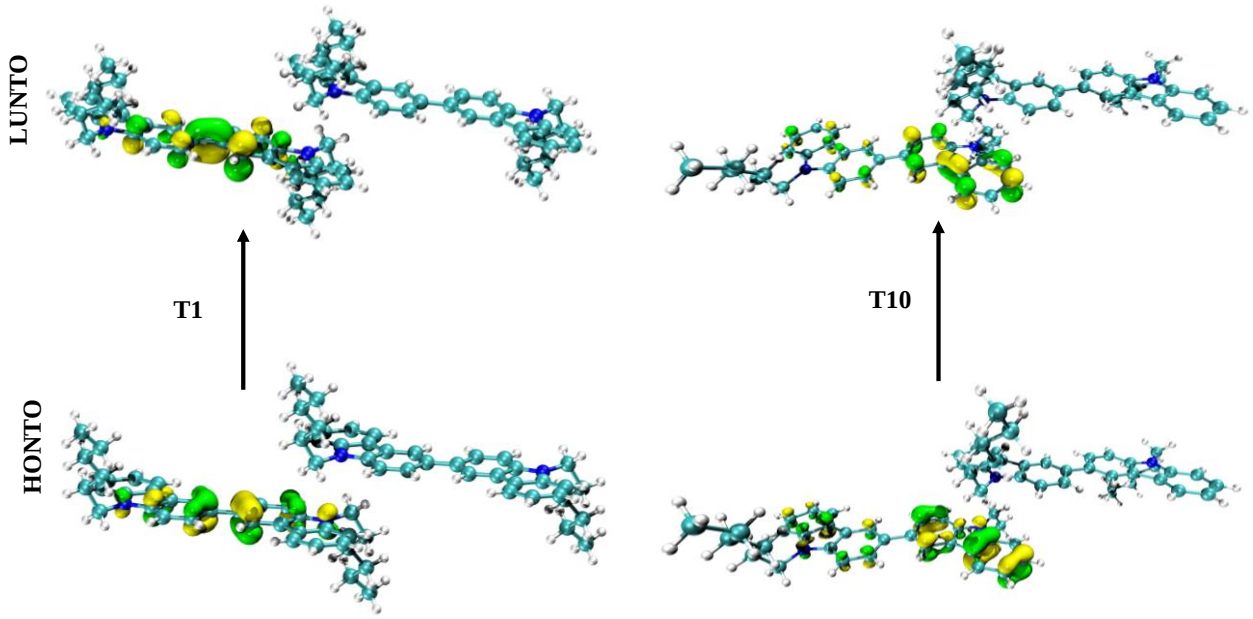

Figure S23: NTO analysis of T1 and T10 energy levels.

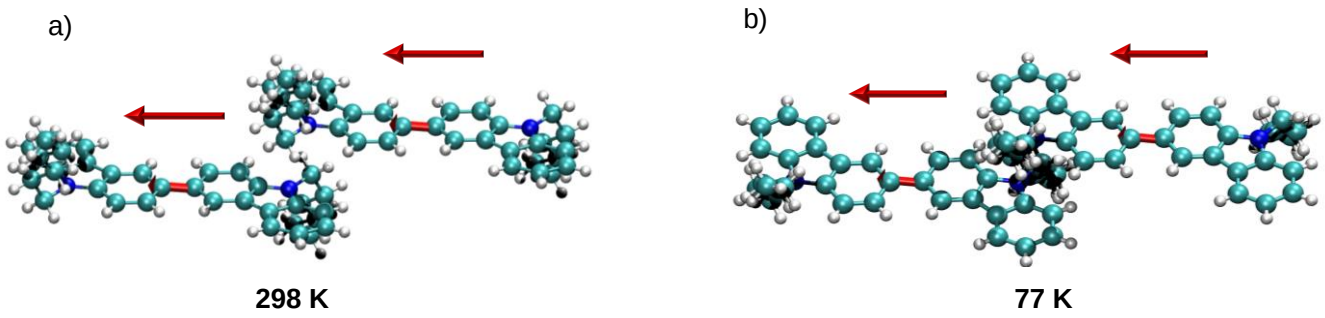

Figure S24: TDM vectors of the two carbazole units adopt a parallel alignment at 298 K, and at 77 K for S_5 electronic energy level.

Section 6: Appendix Figures

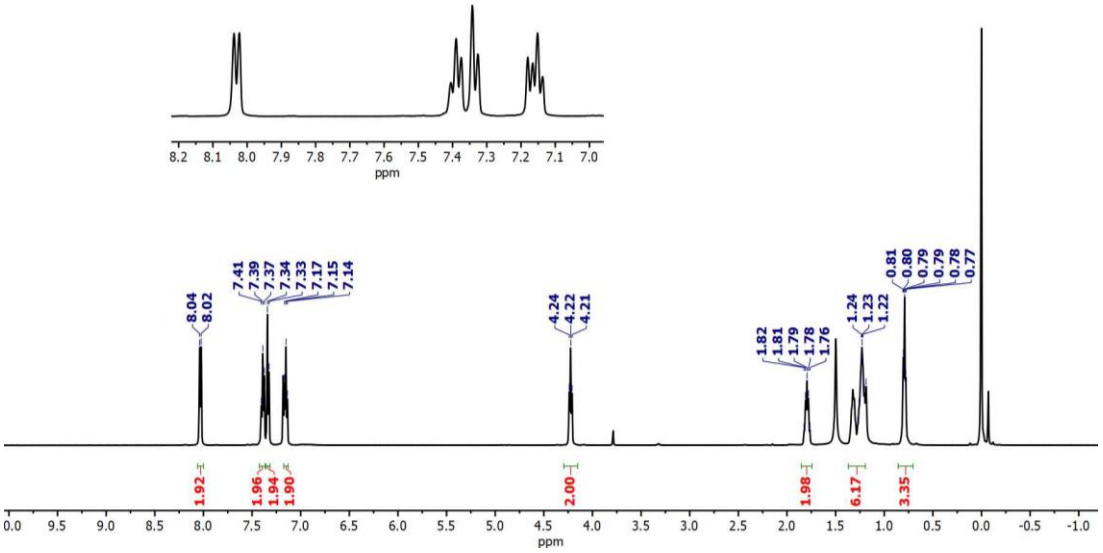

Figure A1: ^{1}H-NMR spectra of N-hexyl carbazole.

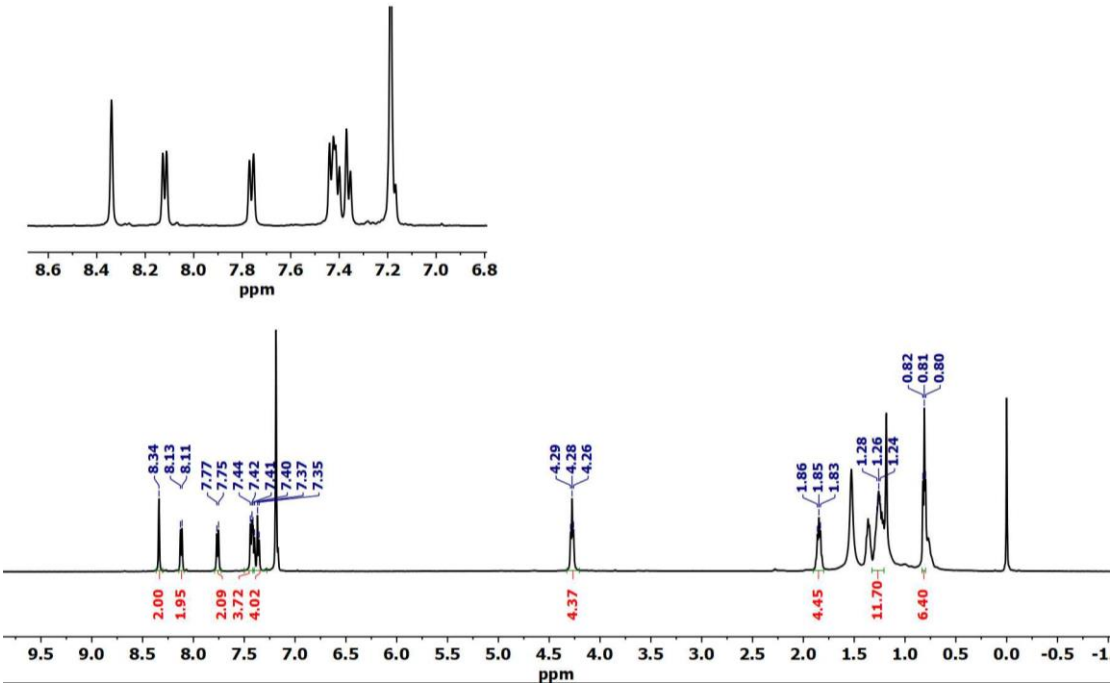

Figure A2: ^{1}H-NMR spectra of **CD**.

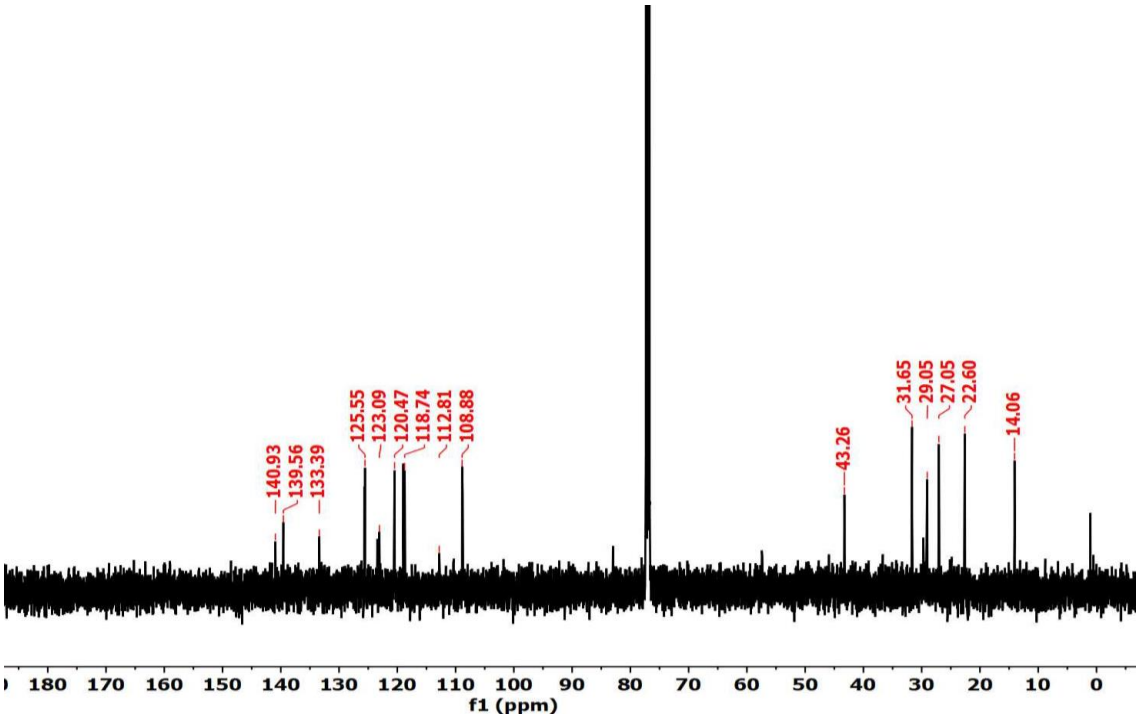

Figure A3: ^{13}C-NMR spectra of **CD**.

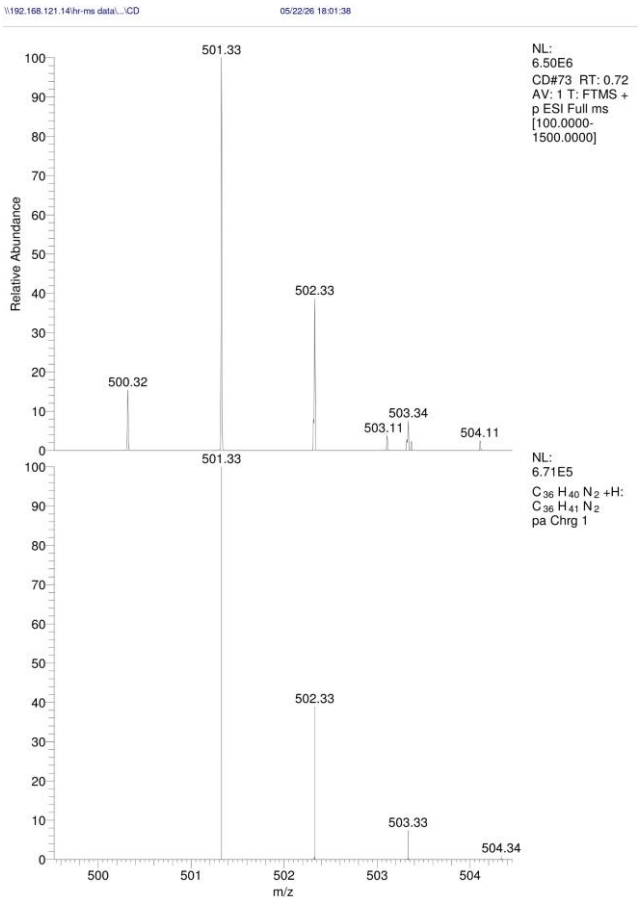

Figure A4: HRMS spectra of **CD**

Coordinates

N 4.89780000 6.14670000 6.52630000
C 4.53740000 7.42430000 8.38340000
C 5.39230000 8.16320000 7.48270000
C 4.00400000 7.70850000 9.63910000
H 4.21000000 8.53220000 10.06510000
C 5.59400000 7.33300000 6.35830000
C 3.16650000 6.78560000 10.27530000
C 2.88510000 5.57790000 9.59850000
H 2.30800000 4.94950000 10.01620000
C 4.24790000 6.19550000 7.74690000
C 5.87540000 4.09330000 5.47670000
H 6.74450000 4.56620000 5.44320000
H 5.79610000 3.55110000 4.65220000
C 4.75470000 5.12580000 5.49540000
H 4.71800000 5.57030000 4.61160000
H 3.89340000 4.65680000 5.63090000
C 6.68740000 0.94720000 7.63710000
H 7.03050000 1.35210000 8.47280000
H 5.73340000 0.72270000 7.77760000
C 6.36660000 7.74280000 5.27120000
H 6.51090000 7.17360000 4.52440000
C 5.95040000 9.44180000 7.50570000
H 5.81200000 10.01650000 8.24940000
C 6.80090000 1.96230000 6.50620000
H 6.59020000 1.51420000 5.64890000
H 7.73520000 2.28590000 6.45660000
C 3.40990000 5.26620000 8.35560000
H 3.20380000 4.44180000 7.93070000
C 6.71190000 9.85920000 6.42200000
H 7.09870000 10.72690000 6.42500000
C 6.91460000 9.01410000 5.32590000
H 7.44310000 9.32050000 4.59830000
C 5.87040000 3.15780000 6.68300000
H 6.14630000 3.66580000 7.48670000
H 4.94850000 2.83010000 6.83370000
C 7.46370000 -0.33040000 7.34540000
H 7.11100000 -0.74850000 6.53220000
H 7.36840000 -0.94980000 8.09890000
H 8.41110000 -0.11500000 7.21750000
N 0.85400000 7.70150000 15.36440000
C 1.21440000 6.42390000 13.50730000

C 0.35950000 5.68500000 14.40800000
C 1.74770000 6.13970000 12.25150000
H 1.54170000 5.31600000 11.82560000
C 0.15770000 6.51520000 15.53240000
C 2.58520000 7.06260000 11.61540000
C 2.86670000 8.27030000 12.29220000
H 3.44370000 8.89870000 11.87440000
C 1.50380000 7.65270000 14.14380000
C -0.12360000 9.75490000 16.41390000
H -0.99270000 9.28200000 16.44750000
H -0.04440000 10.29710000 17.23850000
C 0.99710000 8.72240000 16.39520000
H 1.03370000 8.27790000 17.27910000
H 1.85830000 9.19140000 16.25980000
C -0.93560000 12.90100000 14.25360000
H -1.27880000 12.49610000 13.41790000
H 0.01830000 13.12550000 14.11300000
C -0.61480000 6.10540000 16.61950000
H -0.75910000 6.67460000 17.36630000
C -0.19870000 4.40640000 14.38500000
H -0.06030000 3.83170000 13.64130000
C -1.04910000 11.88590000 15.38440000
H -0.83850000 12.33400000 16.24170000
H -1.98340000 11.56230000 15.43410000
C 2.34190000 8.58200000 13.53510000
H 2.54790000 9.40640000 13.96000000
C -0.96020000 3.98900000 15.46870000
H -1.34700000 3.12130000 15.46570000
C -1.16280000 4.83410000 16.56480000
H -1.69140000 4.52770000 17.29230000
C -0.11870000 10.69040000 15.20770000
H -0.39460000 10.18240000 14.40400000
H 0.80330000 11.01810000 15.05700000
C -1.71190000 14.17860000 14.54520000
H -1.35930000 14.59670000 15.35840000
H -1.61660000 14.79800000 13.79180000
H -2.65940000 13.96320000 14.67310000

References

(1) Caricato, M.; Frisch, M. J.; Hiscocks, J.; Frisch, M. J. *Gaussian 09: IOps Reference*; Gaussian Wallingford, CT, USA, 2009.

(2) Tonge, K. H. Potential energy surfaces. *Journal of Chemical Education* **1988**, *65* (*1*), 65.

(3) Sheldrick, G. M. A short history of SHELX. *Foundations of crystallography* **2008**, *64* (*1*), 112-122.

(4) Farrugia, L. J. WinGX suite for small-molecule single-crystal crystallography. *J. Appl. Cryst.* **1999**, *32* (*4*), 837-838.

(5) Macrae, C. F.; Sovago, I.; Cottrell, S. J.; Galek, P. T.; McCabe, P.; Pidcock, E.; Platings, M.; Shields, G. P.; Stevens, J. S.; Towler, M. Mercury 4.0: From visualization to analysis, design and prediction. *Appl. Cryst.* **2020**, *53* (*1*), 226-235.

(6) Hohenstein, E. G.; Sherrill, C. D. Wavefunction methods for noncovalent interactions. *Wiley Interdisciplinary Reviews: Computational Molecular Science* **2012**, *2* (*2*), 304-326. Hohenstein, E. G.; Parrish, R. M.; Sherrill, C. D.; Turney, J. M.; Schaefer, H. F. Large-scale symmetry-adapted perturbation theory computations via density fitting and Laplace transformation techniques: Investigating the fundamental forces of DNA-intercalator interactions. *J. chem. phys.* **2011**, *135* (*17*).

(7) JJ, S. P. T. M. M. Wolff SK Grimwood DJ Jayatilaka D. *Spackman MA J. Appl. Crystallogr* **2021**, *54* (*3*), 1006-1011.

(8) Spackman, M. A.; Jayatilaka, D. Hirshfeld surface analysis. *CrystEngComm* **2009**, *11* (*1*), 19-32.

(9) You, Z. Q.; Hsu, C. P. Theory and calculation for the electronic coupling in excitation energy transfer. *Int. J. Quantum Chem.* **2014**, *114* (*2*), 102-115.

(10) Scholes, G. D. Long-range resonance energy transfer in molecular systems. *Annual review of physical chemistry* **2003**, *54* (*1*), 57-87.

(11) Mullen, K. M.; Snellenburg, J. J.; Laptenok, S. P.; Snellenburg, M. J. J.; deSolve, I. Package 'TIMP'. **2015**.

(12) Ford, W. E.; Kamat, P. V. Photochemistry of 3, 4, 9, 10-perylenetetracarboxylic dianhydride dyes. 3. Singlet and triplet excited-state properties of the bis (2, 5-di-tert-butylphenyl) imide derivative. *J. Phys. Chem.* **1987**, *91* (*25*), 6373-6380.